

The cold-atom elevator: From edge-state injection to the preparation of fractional Chern insulators

Botao Wang,^{1,*} Monika Aidelsburger,^{2,3,4} Jean Dalibard,⁵ André Eckardt,^{6,†} and Nathan Goldman^{1,‡}

¹*CENOLI, Université Libre de Bruxelles, CP 231, Campus Plaine, B-1050 Brussels, Belgium*

²*Faculty of Physics, Ludwig-Maximilians-Universität München, Schellingstr. 4, D-80799 Munich, Germany*

³*Max-Planck-Institut für Quantenoptik, 85748 Garching, Germany*

⁴*Munich Center for Quantum Science and Technology (MCQST), Schellingstr. 4, D-80799 Munich, Germany*

⁵*Laboratoire Kastler Brossel, Collège de France, CNRS, ENS-PSL University,*

Sorbonne Université, 11 Place Marcelin Berthelot, 75005 Paris, France

⁶*Technische Universität Berlin, Institut für Theoretische Physik, Hardenbergstr. 36, 10623 Berlin, Germany*

(Dated: June 28, 2023)

Optical box traps for cold atoms offer new possibilities for quantum-gas experiments. Building on their exquisite spatial and temporal control, we propose to engineer system-reservoir configurations using box traps, in view of preparing and manipulating topological atomic states in optical lattices. First, we consider the injection of particles from the reservoir to the system: this scenario is shown to be particularly well suited to activate energy-selective chiral edge currents, but also, to prepare fractional Chern insulating ground states. Then, we devise a practical evaporative-cooling scheme to effectively cool down atomic gases into topological ground states. Our open-system approach to optical-lattice settings provides a new path for the investigation of ultracold quantum matter, including strongly-correlated and topological phases.

Introduction. Optical box traps have been demonstrated as a powerful tool in cold-atom experiments [1]. Boxes of different shapes and dimensionalities have been realized for ultracold atoms or molecules [2–6], which led to novel observations including the quantum Joule–Thomson effect [7] and the recurrences of coherence in a quantum many-body system [8]. The gas homogeneity also facilitates the probe of density-related quantities, including the quantum depletion of atomic condensate [9], the low-energy excitation spectrum of ultracold Fermi gases [10], and sound speed in superfluids [11–18]. Besides, box traps have been used for state preparation, leading to the discovery of a novel breather in a 2D Bose gas [19], the deterministic preparation of a Townes soliton [20], and the demonstration of the transition between atomic and molecular condensates [21].

Combined with optical lattices, box potentials allow to study a well-controlled number of atoms trapped in a few lattice sites. This exquisite control opens up new possibilities, such as measuring the growth of entanglement upon a quench [22], or revealing fundamental properties of the Fermi-Hubbard model [23–31] and many-body localization [32–34]. More recently, programmable box traps enabled the generation of large homogeneous systems of more than 2000 atoms, leading to large-scale quantum simulation of out-of-equilibrium dynamics [35–37]. In the context of topological matter, a Laughlin-type fractional quantum Hall (QH) state has been recently realized in a small box filled with strongly interacting bosons [38]. Isolating 1D lattices also allowed for the observation of the symmetry-protected Haldane phase [39] and 1D anyons [40]. Furthermore, the ability of creating optical boxes with sharp boundaries offers an ideal framework to study topological edge modes [41, 42].

Inspired by the possibility of shaping box potentials of arbitrary geometries, combined with the ability to control these dynamically, we propose to use box traps to partition a lattice system into different subregions, separating a “reservoir” region from a “system” of interest. We explore how dynamically tuning the relative energy between these two regions allows for the controlled preparation of interesting states within the system, a scheme coined “cold-atom elevator”. We investigate two main scenarios: (i) injection of particles from the reservoir to the system, so as to populate edge states in an energy-resolved manner [Fig. 1(a)], or to prepare a strongly-interacting topological ground state in the bulk [Fig. 1(b)]; (ii) controlled removal of particles from an excited state (e.g. a thermal metal), performed in a repeated “vacuum-cleaner” manner, in view of cooling the system down to a topological insulating ground-state [Fig. 1(c)]; see also Refs. [43, 44].

Edge-state injection. Partitioning boxes naturally provides sharp boundaries between a system and reservoirs, an ideal platform to realize and probe topological edge states. Hallmark of topologically nontrivial states, chiral edge states have been observed in photonic systems [45–47] and in cold atoms using synthetic dimensions [48–54]. Despite various proposals [55–62], the realization of real-space atomic chiral edge modes has only been reported recently [41, 42]. We now show how our sub-box geometry can be used to activate topological edge currents within an empty system, in an energy-selective manner and without populating the bulk.

The general idea consists in coupling an empty lattice system (potentially hosting QH states) to a reservoir, as sketched in Fig. 1(a). Particles are initially prepared in the reservoir, in a state that can be chosen trivial [63]. We then perform a sudden lift of the reservoir sub-box energy

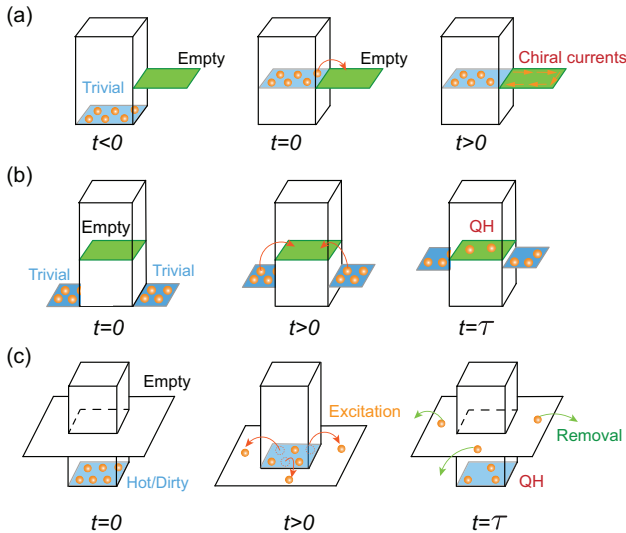


FIG. 1. Sketch of the cold-atom elevator. (a) Protocol for chiral edge state injection. Setting the reservoir energy on resonance with the system’s edge modes, particles are continuously injected into edge states in an energy-selective manner, and chiral edge currents appear in the system without populating the bulk. (b) Injection protocol for state preparation. Starting from a trivial state in the reservoirs, the latter are slowly lifted so as to adiabatically inject particles into the system until an insulating state, e.g. a quantum Hall (QH) state, is formed. (c) Cooling protocol for state preparation. A proper tuning of the reservoir energy can be used to retrieve excitations (hot atoms) from the system. Removing the particles from the reservoir, and repeating this lift-removal process over many cycles, leads to the preparation of the desired insulating (QH) state in the system.

ϵ_R to a *proper* position, such that the energy of the particles in the reservoir becomes resonant with that of the edge mode in the system. In this way, energy-selective edge states will be populated in the initially empty system, allowing for the observation of chiral transport on a dark background.

As a concrete example, we consider the Harper-Hofstadter (HH) model [64], a square lattice with magnetic flux $\phi = 2\pi\alpha$ per plaquette, coupled to reservoirs:

$$\hat{H} = - \sum_{\langle \ell \ell' \rangle} \left(J_{\ell \ell'} e^{i\phi_{\ell \ell'}} \hat{a}_{\ell}^{\dagger} \hat{a}_{\ell'} + \text{h.c.} \right) + \sum_{\ell} \epsilon_{\ell} \hat{n}_{\ell}, \quad (1)$$

where \hat{a}_{ℓ} (\hat{a}_{ℓ}^{\dagger}) are the annihilation (creation) operators on site ℓ and $\hat{n}_{\ell} = \hat{a}_{\ell}^{\dagger} \hat{a}_{\ell}$. We consider nearest-neighbor tunneling amplitudes $J_{\ell \ell'}$ and Peierls phases $\phi_{\ell \ell'}$, and set $\epsilon_{\ell} = \epsilon_R$ in the reservoir (zero otherwise). Whether the reservoir is also subjected to the flux or not does not qualitatively change our findings [63], hence, for simplicity, we suppose that the entire system-reservoir setting is described by the HH model: we set $J_{\ell \ell'} = 1$ and choose Peierls phases $\phi_{\ell \ell'} = \phi n$ (resp. 0) for hopping along x (resp. y), where n is the lattice index along y .

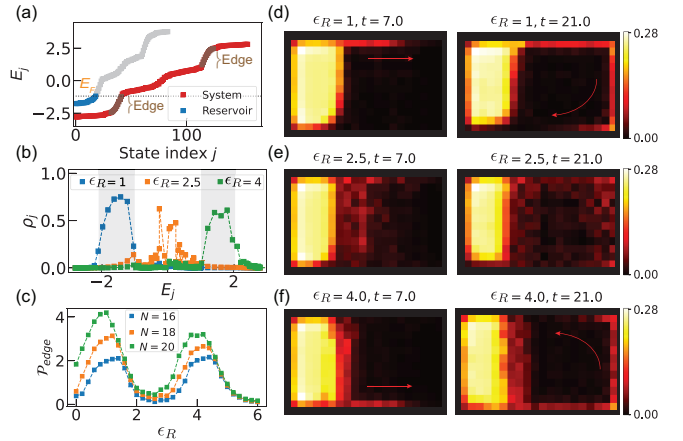


FIG. 2. Edge state injection in the HH model. (a) Spectrum as a function of the eigenstate index j . The blue and red dots correspond to the Hamiltonian describing the reservoir (with $\epsilon_R = 1$) and the system, respectively. E_F denotes the Fermi energy. (b) Population of HH eigenstates ρ_j as a function of their energy E_j , at time $t = 28$. (c) Edge-mode population as a function of ϵ_R for different initial particle number N in the reservoir. Snapshots of spatial density distribution for (d) $\epsilon_R = 1$, (e) $\epsilon_R = 2.5$, (f) $\epsilon_R = 4$ at times $t = 7, 21$. Here, a system of size 13×12 and with flux $\phi = \pi/2$ per plaquette is coupled to a reservoir of size 7×12 . Except for (c), the number of particles is $N = 19$. Energy and time are in units of J and \hbar/J , respectively. The arrows in (d) and (f) are a guide to the eye for the chiral motion.

The HH Hamiltonian is a paradigmatic model of Chern insulators (CIs): it hosts topologically nontrivial energy bands, which are characterized by nonzero Chern numbers [65]. Setting open boundary conditions (OBC), the model hosts chiral edge modes within the bulk energy gaps [58, 59, 63]. We show the energy spectrum for a system of size 13×12 and a reservoir of size 7×12 in Fig. 2(a); the regions of low density of states (steeper slopes), correspond to chiral edge states. When setting the lift energy to the value $\epsilon_R = 1$, the states populated in the reservoir become resonant with the chiral edge states located within the lowest bulk gap of the system.

Based on this observation, we show how to populate edge states in an energy-selective manner. We start with $N = 19$ particles in the reservoir, which corresponds to a complete filling of its nearly-flat lowest Bloch band; the flatness allows for energy-selective population of system states. We investigate the quench dynamics obtained by solving the time-dependent Schrödinger equation, using different values of ϵ_R . For $\epsilon_R = 1$, a clockwise chiral edge current is clearly observed in Fig. 2(d), where we plot the spatial density distribution at different times. When the box potential is lifted to $\epsilon_R = 4$, i.e. when the reservoir is resonant with the edges states located in the upper gap, an opposite chiral motion occurs [Fig. 2(f)]. Setting $\epsilon_R = 2.5$, the populated reservoir states are resonant with the middle Bloch band of the system, in which case bulk

states are populated in the system [Fig. 2(e)].

To quantify our edge-state injection scheme, we define the mean occupation $\rho_j(t)$ of an individual single-particle eigenstate j in the HH system. As shown in Fig. 2(b), we find dominant populations in the bulk gaps for $\epsilon_R = 1$ (lower gap) and $\epsilon_R = 4$ (upper gap). Furthermore, we define the total edge-state population $\mathcal{P}_{\text{edge}} = \sum_{j \in \text{Edge}} \rho_j$, where the state index j runs over all edge modes. Figure 2(c) shows the population $\mathcal{P}_{\text{edge}}$ as a function of ϵ_R at time $t=28$ for different particle numbers N . By lowering the number of fermions in the reservoir, one observes a smaller edge-mode population. In any case, the peak positions clearly indicate the energetic location of the edge modes (strong signal) and bulk modes (weak signal). As a corollary, our edge-state injection scheme can be used as a spectroscopic tool for atomic QH systems.

FCI preparation based on particle injection. A natural question concerns the possibility of using the injection scheme to form an insulating (QH) ground state within the bulk of the system. We first explored this scheme for a system of non-interacting fermions in view of forming a CI, and we present our findings in [63]. Here, we demonstrate the applicability of this scheme to realize a fractional Chern insulator (FCI): a lattice analogue of a fractional QH state [66, 67]. Several schemes have been proposed for realizing FCIs with cold atoms, based on the adiabatic variation of various system parameters [68–77]. Such a scheme was recently implemented to form an FCI state of two strongly-interacting bosons in a 4×4 lattice [38]. We now show that an open-system approach, based on dynamically tuning box potentials, offers an alternative, potentially simpler and better, approach to prepare an FCI ground state with hard-core bosons.

We consider the sub-box configuration depicted in Fig. 1(b): the system is connected to two reservoirs (without flux). The initial state is an easily-prepared trivial state with all (interacting) particles in the reservoirs. The system region, which is initially empty, is described by the Hofstadter-Bose-Hubbard model with hard-core interactions, which is known to host a $\nu = 1/2$ Laughlin-type ground state [78–83]. We aim at gently injecting particles from the reservoirs to the system, by slowly lifting the reservoirs energy, in view of building up an FCI ground state in the system. Here, we set the hopping $J_{\ell\ell'} = J_R < 1$ within the reservoirs and the connecting interface, to limit excitations during preparation.

We first analyze the (static) ground-state properties of our system-reservoir setup, as a function of the reservoirs' energy ϵ_R . Figure 3(c) shows the bulk density n_B , as evaluated within the central 2×2 sites. The incompressible nature of the FCI state clearly manifests as a plateau in the bulk density. In contrast to more conventional closed-system schemes, the present system automatically chooses the ideal number of bosons to form the FCI state (for the given flux value and number of lattice sites). The density reaches $n_B \approx 0.18$ on the plateau, and we verified

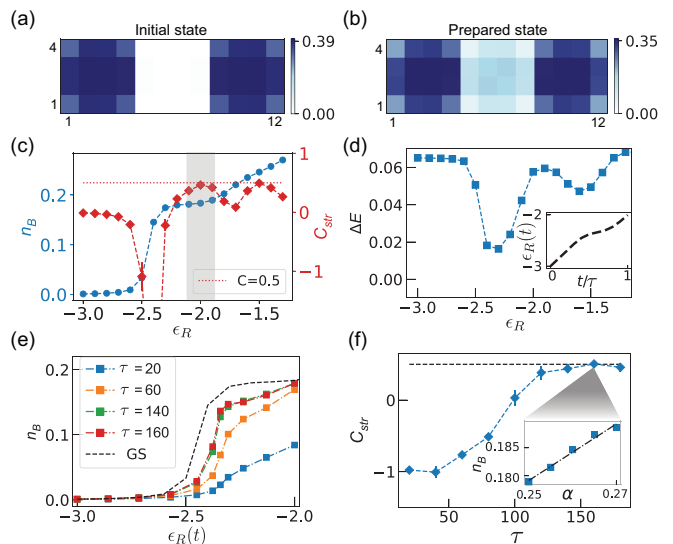


FIG. 3. Preparing a fractional Chern insulator based on injection. (a) Spatial density distribution of the initial state with $\epsilon_R = -3$. (b) Density distribution of the prepared state using the ramp shown in the inset of panel (d) and $\tau = 160$. (c) Bulk density and the local Středa marker as a function of ϵ_R . The shadow indicates the FCI regime. (d) Many-body energy gap as a function of ϵ_R . Inset: the ramping protocol of $\epsilon_R(t)$ from -3 to -2 within time τ . (e) Bulk density as a function of ϵ_R for different τ and for the instantaneous ground state. (f) Local marker as a function of τ . Inset: linear fit of the density versus flux at $\tau = 160$, which gives $C_{\text{str}} = 0.51$. Here, we consider $N=12$ hard-core bosons; the system of size 4×4 is coupled to two reservoirs of size 4×4 , with $J_R = 0.15$. The error bars denote the standard error of the regression slope used to extract C_{str} in Eq. (2).

that it converges towards the thermodynamic prediction $n_B = 1/8$ for increasing system sizes [63]. As another hallmark signature of the FCI, we evaluate the fractionally-quantized Hall conductivity σ_H , which is encoded in the density distribution via Středa's formula [83–87],

$$C_{\text{str}} = \frac{\partial n_B}{\partial \alpha} = \frac{\sigma_H}{\sigma_0}, \quad (2)$$

where $\sigma_0 = 1/2\pi$ is the conductivity quantum. For a $\nu = 1/2$ Laughlin state, the Středa marker is expected to take the value $C_{\text{str}} = 1/2$, which is the many-body Chern number of the state. In our case, we find $C_{\text{str}} \simeq 0.46$ at $\epsilon_R = -2$, hence indicating the precursor of a fractional Hall response [Fig. 3(c)]. It is interesting to compare this result to the value $C'_{\text{str}} = 0.61$, which is obtained in the experimental closed-box configuration of Ref. [38], where an exact number of bosons ($N = 2$) is loaded in 4×4 sites; this comparison supports the idea that the system optimizes the formation of an FCI state when coupled to reservoirs.

The bulk density and the Středa marker both show an interesting behavior across the transition that occurs within the system, as particles enter the system and even-

tually form the FCI state. Indeed, in the vicinity of $\epsilon_R \approx -2.5$, one notices an abrupt increase in n_B and a breakdown of Středa's formula [Fig. 3(c)], accompanied with a sudden drop in the many-body gap [Fig. 3(d)]. The minimal many-body gap associated with this transition is $\Delta = 0.016$, which suggests a realistic ramping time $\tau \sim 100$ for adiabatic state preparation, compatible with recent experiments [38].

We now analyze how an FCI ground state can be dynamically prepared by slowly ramping up the reservoir energy to the ideal value $\epsilon_R \approx -2$. To optimize adiabatic preparation, we adjust the ramp according to the many-body gap; see the inset in Fig. 3(d). By tracking the bulk density during the ramp [Fig. 3(e)], one recovers the formation of a plateau for a sufficiently long ramping time τ , in agreement with the adiabatic-limit prediction of Fig. 3(c). As further confirmed by the local Středa marker, an FCI ground state with $C_{\text{str}} \approx 0.5$ is prepared for adiabatic times $\tau \gtrsim 140$ [Fig. 3(f)]. The comparison with a less efficient, linear ramp is presented in Ref. [63].

State preparation via repeated cleaning. So far, we have discussed a protocol by which particles are injected from a reservoir into an empty system. Motivated by the ability of easily preparing an empty reservoir (a trivial zero-entropy state), we now explore the possibility of using the reservoir as a vacuum-cleaning resource in view of preparing ground states in the system. As sketched in Fig. 1(c), one considers a ‘dirty’ (excited) initial state within our system. The cleaning cycle is then as follows: (i) we slowly lower the reservoir energy, such as to retrieve excitations (hot atoms) from the system in a controlled manner; (ii) after this cleaning process, one rapidly lifts the reservoir until it becomes decoupled from the system; and (iii) one completely empties the reservoir. This cleaning cycle is then repeated n_{cyc} times, until convergence is reached towards a target insulating (QH) state within the box. The advantage of this scheme is two-fold: the empty reservoir state can be viewed as a perfect and easy-to-prepare zero-temperature state of holes; the difficulty in removing particles that are located deep in the bulk is compensated by several repetitions.

We apply this scheme to a concrete preparation sequence, designed to prepare Chern insulators in atomic HH systems. Inspired by Ref. [88], we start from a trivial metal realized by loading non-interacting fermions in a square lattice at half-filling in the presence of a staggered potential [63]. We then ramp up the flux in the lattice to the value $\phi = \pi/2$, while reducing the staggered potential, hence changing the topological nature of the bands: at the end of this sequence, the target lowest band has a Chern number $C = 1$. Due to the occupation of higher bands in the initial metallic state, the target (lowest) band remains perfectly filled during the whole duration of this sequence, despite the gap closing ($C = 0 \rightarrow 1$). The (irregular) band populations, obtained at the end of this sequence, are shown by blue dots in Fig. 4(b).

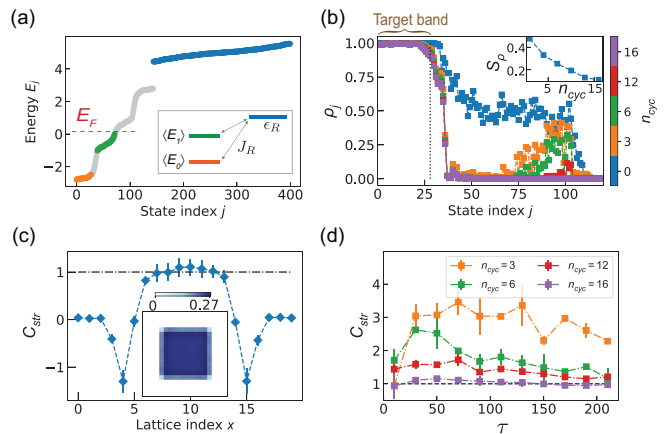


FIG. 4. Preparing a Chern insulator by using the lift-removal strategy. (a) Energy spectrum of the HH model coupled to a trivial reservoir. Here, we partition a lattice of size 20×20 into a target 12×12 system (central box) and a surrounding reservoir. E_F denotes the Fermi energy. We set a flux $\phi = \pi/2$ in the system only. Inset: Simplified three-level model; $\langle E_0 \rangle$ and $\langle E_1 \rangle$ denote representative energies of the lowest two bands. (b) Population in HH eigenstates ρ_j for different n_{cyc} . Inset: the HH orbital entropy versus n_{cyc} . We set $J_R = 0.15$ and $\tau = 90$ per cycle. (c) The local Středa marker of the evolved state at $n_{\text{cyc}} = 16$, as a function of the site index along the middle row. Inset: the corresponding spatial density distribution of the evolved state. (d) The local marker as a function of τ for different cycles n_{cyc} . The local marker is averaged over a disk at the center with a radius of $r = 2$. The error bars denote the standard error of the regression slope used to extract C_{str} .

Our aim is to remove atoms from higher bands, while leaving the lowest Chern band ($C = 1$) almost perfectly filled, in view of forming a CI in the system. To achieve this goal, we now apply our vacuum-cleaning protocol by dynamically tuning the reservoir energy ϵ_R . During each cycle of duration τ , we vary $\epsilon_R(t)$ with a saturation function [63], using a large initial value $\epsilon_R^i = 4$. At the end of this first cycle, $\epsilon_R(t)$ reaches the value $\epsilon_R^f = -1.14$, which is located right below the first excited Bloch band of the system. After lowering the reservoir to the final value ϵ_R^f , we then quickly lift it up until it becomes effectively decoupled from the system; we then empty the reservoir and complete one cycle. We then repeat this cleaning sequence, but for the sake of efficiency, we progressively increase the final value ϵ_R^f at each cycle to properly address all the higher bands [63]. We note that this cleaning scheme can be understood through a simplified 3-level toy model [inset of Fig. 4(a)], which can serve as a guide in view of optimizing the control parameters [63].

Figure 4(b) demonstrates the efficient depletion of the excited bands (and the resulting decrease of entropy) as a function of the cycle number n_{cyc} . In this process, the bulk states of the lowest band remain almost perfectly filled, and we find that a satisfactory CI ground state is formed after 16 cycles of duration $\tau = 90$. We plot

the local (single-site) Středa marker in Fig. 4(c), which confirms the topological nature of the bulk, $C_{\text{str}} \approx 1$. We plot C_{str} as a function of the ramping time per cycle for different n_{cyc} in Fig. 4(d). This shows that an efficient cleaning is reached for $n_{\text{cyc}} \approx 12$ cycles of duration $\tau \gtrsim 200$, and for $n_{\text{cyc}} \approx 16$ cycles of duration $\tau \gtrsim 50$.

Concluding remarks. This work explored different possibilities offered by the design of tunable boxes in cold-atom experiments, setting the focus on the realization of topological states. This approach offers substantial advantages: it relies on the preparation of a simple initial state in the reservoir and the ability to dynamically tune the latter's energy relative to the system region. In this sense, our open-system approach does not require any fine-tuning nor complicated time-dependence of the system parameters, and it is readily applicable to create a broad class of (bosonic or fermionic) many-body states of interest, including exotic Mott insulators and antiferromagnetic states in Hubbard-type models. While we considered a spatial separation between the system and reservoir regions on the 2D plane, we note that a double-layer configuration could also be envisaged to further enhance the transfer of particles between the two regions; this could be realized using a bilayer optical lattice or by exploiting two laser-coupled internal states of an atom. Finally, it would be interesting to combine the injection and cleaning schemes presented in this work, in view of realizing large FCI states or to explore quantum thermodynamics.

Acknowledgments. The authors thank Julian Leonard, Yanfei Li, Nir Navon, Cecile Repellin, Raphael Saint-Jalm, Perrin Segura, Boye Sun, Amit Vashisht and Christof Weitenberg for discussions. J.D. acknowledges the support of the Solvay Institutes, within the framework of the Jacques Solvay International Chairs in Physics. Work in Brussels is also supported by the FRS-FNRS (Belgium), the ERC Starting Grants TopoCold and LATIS, and the EOS project CHEQS. M.A. and A.E. acknowledge support from the Deutsche Forschungsgemeinschaft (DFG) via the Research Unit FOR 2414 under Project No. 277974659. M.A. also acknowledges funding from the DFG under Germany's Excellence Strategy – EXC-2111 – 390814868.

* botao.wang@ulb.be

† eckardt@tu-berlin.de

‡ nathan.goldman@ulb.be

- [1] N. Navon, R. P. Smith, and Z. Hadzibabic, Quantum gases in optical boxes, *Nature Physics* **17**, 1334 (2021).
 [2] A. L. Gaunt, T. F. Schmidutz, I. Gotlibovych, R. P. Smith, and Z. Hadzibabic, Bose-einstein condensation of atoms in a uniform potential, *Phys. Rev. Lett.* **110**, 200406 (2013).
 [3] L. Chomaz, L. Corman, T. Bienaimé, R. Desbuquois,

- C. Weitenberg, S. Nascimbene, J. Beugnon, and J. Dalibard, Emergence of coherence via transverse condensation in a uniform quasi-two-dimensional bose gas, *Nature communications* **6**, 6162 (2015).
 [4] B. Mukherjee, Z. Yan, P. B. Patel, Z. Hadzibabic, T. Yefsah, J. Struck, and M. W. Zwierlein, Homogeneous atomic fermi gases, *Phys. Rev. Lett.* **118**, 123401 (2017).
 [5] K. Hueck, N. Luick, L. Sobirey, J. Siegl, T. Lompe, and H. Moritz, Two-dimensional homogeneous fermi gases, *Phys. Rev. Lett.* **120**, 060402 (2018).
 [6] R. Bause, A. Schindewolf, R. Tao, M. Duda, X.-Y. Chen, G. Quémener, T. Karman, A. Christianen, I. Bloch, and X.-Y. Luo, Collisions of ultracold molecules in bright and dark optical dipole traps, *Phys. Rev. Res.* **3**, 033013 (2021).
 [7] T. F. Schmidutz, I. Gotlibovych, A. L. Gaunt, R. P. Smith, N. Navon, and Z. Hadzibabic, Quantum joule-thomson effect in a saturated homogeneous bose gas, *Phys. Rev. Lett.* **112**, 040403 (2014).
 [8] B. Rauer, S. Erne, T. Schweigler, F. Cataldini, M. Tajik, and J. Schmiedmayer, Recurrences in an isolated quantum many-body system, *Science* **360**, 307 (2018).
 [9] R. Lopes, C. Eigen, N. Navon, D. Clément, R. P. Smith, and Z. Hadzibabic, Quantum depletion of a homogeneous bose-einstein condensate, *Phys. Rev. Lett.* **119**, 190404 (2017).
 [10] H. Biss, L. Sobirey, N. Luick, M. Bohlen, J. J. Kinnunen, G. M. Bruun, T. Lompe, and H. Moritz, Excitation spectrum and superfluid gap of an ultracold fermi gas, *Phys. Rev. Lett.* **128**, 100401 (2022).
 [11] N. Navon, A. L. Gaunt, R. P. Smith, and Z. Hadzibabic, Emergence of a turbulent cascade in a quantum gas, *Nature* **539**, 72 (2016).
 [12] J. L. Ville, R. Saint-Jalm, E. Le Cerf, M. Aidelsburger, S. Nascimbène, J. Dalibard, and J. Beugnon, Sound propagation in a uniform superfluid two-dimensional bose gas, *Phys. Rev. Lett.* **121**, 145301 (2018).
 [13] L. Baird, X. Wang, S. Roof, and J. E. Thomas, Measuring the hydrodynamic linear response of a unitary fermi gas, *Phys. Rev. Lett.* **123**, 160402 (2019).
 [14] P. B. Patel, Z. Yan, B. Mukherjee, R. J. Fletcher, J. Struck, and M. W. Zwierlein, Universal sound diffusion in a strongly interacting fermi gas, *Science* **370**, 1222 (2020).
 [15] M. Bohlen, L. Sobirey, N. Luick, H. Biss, T. Enss, T. Lompe, and H. Moritz, Sound propagation and quantum-limited damping in a two-dimensional fermi gas, *Phys. Rev. Lett.* **124**, 240403 (2020).
 [16] S. J. Garratt, C. Eigen, J. Zhang, P. Turzák, R. Lopes, R. P. Smith, Z. Hadzibabic, and N. Navon, From single-particle excitations to sound waves in a box-trapped atomic bose-einstein condensate, *Phys. Rev. A* **99**, 021601 (2019).
 [17] P. Christodoulou, M. Gałka, N. Dogra, R. Lopes, J. Schmitt, and Z. Hadzibabic, Observation of first and second sound in a bkt superfluid, *Nature* **594**, 191 (2021).
 [18] J. Zhang, C. Eigen, W. Zheng, J. A. P. Glidden, T. A. Hilker, S. J. Garratt, R. Lopes, N. R. Cooper, Z. Hadzibabic, and N. Navon, Many-body decay of the gapped lowest excitation of a bose-einstein condensate, *Phys. Rev. Lett.* **126**, 060402 (2021).
 [19] R. Saint-Jalm, P. C. M. Castilho, E. Le Cerf, B. Bakkali-Hassani, J.-L. Ville, S. Nascimbene, J. Beugnon, and J. Dalibard, Dynamical symmetry and breathers in a two-

- dimensional bose gas, *Phys. Rev. X* **9**, 021035 (2019).
- [20] B. Bakkali-Hassani, C. Maury, Y.-Q. Zou, E. Le Cerf, R. Saint-Jalm, P. C. M. Castilho, S. Nascimbene, J. Dalibard, and J. Beugnon, Realization of a townes soliton in a two-component planar bose gas, *Phys. Rev. Lett.* **127**, 023603 (2021).
- [21] Z. Zhang, L. Chen, K.-X. Yao, and C. Chin, Transition from an atomic to a molecular bose–einstein condensate, *Nature* **592**, 708 (2021).
- [22] R. Islam, R. Ma, P. M. Preiss, M. E. Tai, A. Lukin, M. Rispoli, and M. Greiner, Measuring entanglement entropy in a quantum many-body system, *Nature* **528**, 77 (2015).
- [23] M. F. Parsons, A. Mazurenko, C. S. Chiu, G. Ji, D. Greif, and M. Greiner, Site-resolved measurement of the spin-correlation function in the fermi-hubbard model, *Science* **353**, 1253 (2016).
- [24] A. Mazurenko, C. S. Chiu, G. Ji, M. F. Parsons, M. Kanász-Nagy, R. Schmidt, F. Grusdt, E. Demler, D. Greif, and M. Greiner, A cold-atom fermi–hubbard antiferromagnet, *Nature* **545**, 462 (2017).
- [25] C. S. Chiu, G. Ji, A. Mazurenko, D. Greif, and M. Greiner, Quantum state engineering of a hubbard system with ultracold fermions, *Phys. Rev. Lett.* **120**, 243201 (2018).
- [26] C. S. Chiu, G. Ji, A. Bohrdt, M. Xu, M. Knap, E. Demler, F. Grusdt, M. Greiner, and D. Greif, String patterns in the doped hubbard model, *Science* **365**, 251 (2019).
- [27] J. Koepsell, J. Vijayan, P. Sompet, F. Grusdt, T. A. Hilker, E. Demler, G. Salomon, I. Bloch, and C. Gross, Imaging magnetic polarons in the doped fermi–hubbard model, *Nature* **572**, 358 (2019).
- [28] J. Vijayan, P. Sompet, G. Salomon, J. Koepsell, S. Hirthe, A. Bohrdt, F. Grusdt, I. Bloch, and C. Gross, Time-resolved observation of spin-charge deconfinement in fermionic hubbard chains, *Science* **367**, 186 (2020).
- [29] M. Gall, N. Wurz, J. Samland, C. F. Chan, and M. Köhl, Competing magnetic orders in a bilayer hubbard model with ultracold atoms, *Nature* **589**, 40 (2021).
- [30] S. Hirthe, T. Chalopin, D. Bourgund, P. Bojović, A. Bohrdt, E. Demler, F. Grusdt, I. Bloch, and T. A. Hilker, Magnetically mediated hole pairing in fermionic ladders of ultracold atoms, *Nature* **613**, 463 (2023).
- [31] M. Xu, L. H. Kendrick, A. Kale, Y. Gang, G. Ji, R. T. Scalettar, M. Lebrat, and M. Greiner, Doping a frustrated fermi-hubbard magnet, arXiv:2212.13983 (2022).
- [32] A. Lukin, M. Rispoli, R. Schittko, M. E. Tai, A. M. Kaufman, S. Choi, V. Khemani, J. Leonard, and M. Greiner, Probing entanglement in a many-body-localized system, *Science* **364**, 256 (2019).
- [33] M. Rispoli, A. Lukin, R. Schittko, S. Kim, M. E. Tai, J. Léonard, and M. Greiner, Quantum critical behaviour at the many-body localization transition, *Nature* **573**, 385 (2019).
- [34] J. Léonard, S. Kim, M. Rispoli, A. Lukin, R. Schittko, J. Kwan, E. Demler, D. Sels, and M. Greiner, Probing the onset of quantum avalanches in a many-body localized system, *Nature Physics* **19**, 481 (2023).
- [35] D. Wei, A. Rubio-Abadal, B. Ye, F. Machado, J. Kemp, K. Srakaew, S. Hollerith, J. Rui, S. Gopalakrishnan, N. Y. Yao, *et al.*, Quantum gas microscopy of kardar-parisi-zhang superdiffusion, *Science* **376**, 716 (2022).
- [36] A. Impertro, J. F. Wienand, S. Häfele, H. von Raven, S. Hubele, T. Klostermann, C. R. Cabrera, I. Bloch, and M. Aidelsburger, An unsupervised deep learning algorithm for single-site reconstruction in quantum gas microscopes, arXiv preprint arXiv:2212.11974 (2022).
- [37] J. F. Wienand, S. Karch, A. Impertro, C. Schweizer, E. McCulloch, R. Vasseur, S. Gopalakrishnan, M. Aidelsburger, and I. Bloch, Emergence of fluctuating hydrodynamics in chaotic quantum systems, arXiv preprint arXiv:2306.11457 (2023).
- [38] J. Léonard, S. Kim, J. Kwan, P. Segura, F. Grusdt, C. Repellin, N. Goldman, and M. Greiner, Realization of a fractional quantum hall state with ultracold atoms, arXiv:2210.10919 (2022).
- [39] P. Sompet, S. Hirthe, D. Bourgund, T. Chalopin, J. Bibo, J. Koepsell, P. Bojović, R. Verresen, F. Pollmann, G. Salomon, *et al.*, Realizing the symmetry-protected haldane phase in fermi–hubbard ladders, *Nature* **606**, 484 (2022).
- [40] J. Kwan, P. Segura, Y. Li, S. Kim, A. V. Gorshkov, A. Eckardt, B. Bakkali-Hassani, and M. Greiner, Realization of 1d anyons with arbitrary statistical phase, arXiv:2306.01737 (2023).
- [41] C. Braun, R. Saint-Jalm, A. Hesse, J. Arceri, I. Bloch, and M. Aidelsburger, Real-space detection and manipulation of topological edge modes with ultracold atoms, arXiv:2304.01980 (2023).
- [42] R. Yao, S. Chi, B. Mukherjee, A. Shaffer, M. Zwierlein, and R. J. Fletcher, Observation of chiral edge transport in a rapidly-rotating quantum gas, arXiv:2304.10468 (2023).
- [43] J.-S. Bernier, C. Kollath, A. Georges, L. De Leo, F. Gerbier, C. Salomon, and M. Köhl, Cooling fermionic atoms in optical lattices by shaping the confinement, *Phys. Rev. A* **79**, 061601 (2009).
- [44] T.-L. Ho and Q. Zhou, Squeezing out the entropy of fermions in optical lattices, *Proceedings of the National Academy of Sciences* **106**, 6916 (2009).
- [45] M. C. Rechtsman, J. M. Zeuner, Y. Plotnik, Y. Lumer, D. Podolsky, F. Dreisow, S. Nolte, M. Segev, and A. Szameit, Photonic floquet topological insulators, *Nature* **496**, 196 (2013).
- [46] M. Hafezi, S. Mittal, J. Fan, A. Migdall, and J. Taylor, Imaging topological edge states in silicon photonics, *Nature Photonics* **7**, 1001 (2013).
- [47] T. Ozawa, H. M. Price, A. Amo, N. Goldman, M. Hafezi, L. Lu, M. C. Rechtsman, D. Schuster, J. Simon, O. Zilberberg, and I. Carusotto, Topological photonics, *Rev. Mod. Phys.* **91**, 015006 (2019).
- [48] M. Mancini, G. Pagano, G. Cappellini, L. Livi, M. Rider, J. Catani, C. Sias, P. Zoller, M. Inguscio, M. Dalmonte, and L. Fallani, Observation of chiral edge states with neutral fermions in synthetic Hall ribbons, *Science* **349**, 1510 (2015).
- [49] B. K. Stuhl, H.-I. Lu, L. M. Aycock, D. Genkina, and I. B. Spielman, Visualizing edge states with an atomic bose gas in the quantum Hall regime, *Science* **349**, 1514 (2015).
- [50] L. F. Livi, G. Cappellini, M. Diem, L. Franchi, C. Clivati, M. Frittelli, F. Levi, D. Calonico, J. Catani, M. Inguscio, and L. Fallani, Synthetic dimensions and spin-orbit coupling with an optical clock transition, *Phys. Rev. Lett.* **117**, 220401 (2016).
- [51] F. A. An, E. J. Meier, and B. Gadway, Direct observation of chiral currents and magnetic reflection in atomic flux lattices, *Sci. Adv.* **3**, 10.1126/sciadv.1602685 (2017).
- [52] E. Lustig, S. Weimann, Y. Plotnik, Y. Lumer, M. A.

- Bandres, A. Szameit, and M. Segev, Photonic topological insulator in synthetic dimensions, *Nature* **567**, 356 (2019).
- [53] T. Chalopin, T. Satoor, A. Evrard, V. Makhalov, J. Dalibard, R. Lopes, and S. Nascimbene, Probing chiral edge dynamics and bulk topology of a synthetic Hall system, *Nature Physics*, **1** (2020).
- [54] T. Ozawa and H. M. Price, Topological quantum matter in synthetic dimensions, *Nature Reviews Physics* **1**, 349 (2019).
- [55] N. Goldman, I. Satija, P. Nikolic, A. Bermudez, M. A. Martin-Delgado, M. Lewenstein, and I. Spielman, Realistic time-reversal invariant topological insulators with neutral atoms, *Physical review letters* **105**, 255302 (2010).
- [56] T. D. Stanescu, V. Galitski, and S. D. Sarma, Topological states in two-dimensional optical lattices, *Physical Review A* **82**, 013608 (2010).
- [57] X.-J. Liu, X. Liu, C. Wu, and J. Sinova, Quantum anomalous hall effect with cold atoms trapped in a square lattice, *Physical Review A* **81**, 033622 (2010).
- [58] N. Goldman, J. Beugnon, and F. Gerbier, Detecting chiral edge states in the hofstadter optical lattice, *Physical review letters* **108**, 255303 (2012).
- [59] N. Goldman, J. Dalibard, A. Dauphin, F. Gerbier, M. Lewenstein, P. Zoller, and I. B. Spielman, Direct imaging of topological edge states in cold-atom systems, *Proc. Natl. Acad. Sci. U.S.A.* **110**, 6736 (2013).
- [60] M. D. Reichl and E. J. Mueller, Floquet edge states with ultracold atoms, *Physical Review A* **89**, 063628 (2014).
- [61] N. Goldman, G. Jotzu, M. Messer, F. Görg, R. Desbuquois, and T. Esslinger, Creating topological interfaces and detecting chiral edge modes in a two-dimensional optical lattice, *Phys. Rev. A* **94**, 043611 (2016).
- [62] B. Wang, F. N. Ünal, and A. Eckardt, Floquet engineering of optical solenoids and quantized charge pumping along tailored paths in two-dimensional Chern insulators, *Phys. Rev. Lett.* **120**, 243602 (2018).
- [63] See Supplementary Materials.
- [64] D. R. Hofstadter, Energy levels and wave functions of bloch electrons in rational and irrational magnetic fields, *Phys. Rev. B* **14**, 2239 (1976).
- [65] N. R. Cooper, J. Dalibard, and I. B. Spielman, Topological bands for ultracold atoms, *Rev. Mod. Phys.* **91**, 015005 (2019).
- [66] E. J. Bergholtz and Z. Liu, Topological flat band models and fractional Chern insulators, *International Journal of Modern Physics B* **27**, 1330017 (2013).
- [67] S. A. Parameswaran, R. Roy, and S. L. Sondhi, Fractional quantum Hall physics in topological flat bands, *Comptes Rendus Physique* **14**, 816 (2013).
- [68] M. Popp, B. Paredes, and J. I. Cirac, Adiabatic path to fractional quantum Hall states of a few bosonic atoms, *Phys. Rev. A* **70**, 053612 (2004).
- [69] N. Y. Yao, A. V. Gorshkov, C. R. Laumann, A. M. Läuchli, J. Ye, and M. D. Lukin, Realizing fractional Chern insulators in dipolar spin systems, *Phys. Rev. Lett.* **110**, 185302 (2013).
- [70] E. Kapit, M. Hafezi, and S. H. Simon, Induced self-stabilization in fractional quantum Hall states of light, *Phys. Rev. X* **4**, 031039 (2014).
- [71] F. Grusdt, F. Letscher, M. Hafezi, and M. Fleischhauer, Topological growing of Laughlin states in synthetic gauge fields, *Phys. Rev. Lett.* **113**, 155301 (2014).
- [72] M. Barkeshli, N. Y. Yao, and C. R. Laumann, Continuous preparation of a fractional Chern insulator, *Phys. Rev. Lett.* **115**, 026802 (2015).
- [73] C. Repellin, T. Yefsah, and A. Sterdyniak, Creating a bosonic fractional quantum Hall state by pairing fermions, *Phys. Rev. B* **96**, 161111 (2017).
- [74] J. Motruk and F. Pollmann, Phase transitions and adiabatic preparation of a fractional Chern insulator in a boson cold-atom model, *Phys. Rev. B* **96**, 165107 (2017).
- [75] Y.-C. He, F. Grusdt, A. Kaufman, M. Greiner, and A. Vishwanath, Realizing and adiabatically preparing bosonic integer and fractional quantum Hall states in optical lattices, *Phys. Rev. B* **96**, 201103 (2017).
- [76] A. Hudomal, N. Regnault, and I. Vasić, Bosonic fractional quantum Hall states in driven optical lattices, *Phys. Rev. A* **100**, 053624 (2019).
- [77] B. Andrade, V. Kasper, M. Lewenstein, C. Weitenberg, and T. Graß, Preparation of the $1/2$ Laughlin state with atoms in a rotating trap, *Phys. Rev. A* **103**, 063325 (2021).
- [78] A. S. Sørensen, E. Demler, and M. D. Lukin, Fractional quantum Hall states of atoms in optical lattices, *Phys. Rev. Lett.* **94**, 086803 (2005).
- [79] M. Hafezi, A. S. Sørensen, E. Demler, and M. D. Lukin, Fractional quantum Hall effect in optical lattices, *Phys. Rev. A* **76**, 023613 (2007).
- [80] M. Gerster, M. Rizzi, P. Silvi, M. Dalmonte, and S. Montangero, Fractional quantum Hall effect in the interacting Hofstadter model via tensor networks, *Phys. Rev. B* **96**, 195123 (2017).
- [81] P. Rosson, M. Lubasch, M. Kiffner, and D. Jaksch, Bosonic fractional quantum Hall states on a finite cylinder, *Phys. Rev. A* **99**, 033603 (2019).
- [82] B. Wang, X.-Y. Dong, and A. Eckardt, Measurable signatures of bosonic fractional Chern insulator states and their fractional excitations in a quantum-gas microscope, *SciPost Phys.* **12**, 095 (2022).
- [83] C. Repellin, J. Léonard, and N. Goldman, Fractional Chern insulators of few bosons in a box: Hall plateaus from center-of-mass drifts and density profiles, *Phys. Rev. A* **102**, 063316 (2020).
- [84] A. Widom, Thermodynamic derivation of the hall effect current, *Physics Letters A* **90**, 474 (1982).
- [85] P. Streda, Theory of quantised hall conductivity in two dimensions, *Journal of Physics C: Solid State Physics* **15**, L717 (1982).
- [86] P. Streda and L. Smrcka, Thermodynamic derivation of the hall current and the thermopower in quantising magnetic field, *Journal of Physics C: Solid State Physics* **16**, L895 (1983).
- [87] R. O. Umucalılar, H. Zhai, and M. O. Oktel, Trapped fermi gases in rotating optical lattices: Realization and detection of the topological hofstadter insulator, *Phys. Rev. Lett.* **100**, 070402 (2008).
- [88] M. Aidelsburger, M. Lohse, C. Schweizer, M. Atala, J. T. Barreiro, S. Nascimbène, N. Cooper, I. Bloch, and N. Goldman, Measuring the Chern number of Hofstadter bands with ultracold bosonic atoms, *Nature Physics* **11**, 162 (2015).

Supplementary Material

I. BRIEF REMINDER OF THE HARPER-HOFSTADTER BAND STRUCTURE: EDGE STATES AND CHERN NUMBERS

In this work, we illustrate the cold-atom elevator scheme using the paradigmatic Harper-Hofstadter (HH) model, which describes hopping of particles on a two-dimensional square lattice with a homogenous magnetic flux ϕ per plaquette. The HH Hamiltonian can be written in the Landau gauge as

$$\hat{H} = -J \sum_{m,n} \left(e^{-i\phi n} \hat{a}_{m+1,n}^\dagger \hat{a}_{m,n} + \hat{a}_{m,n+1}^\dagger \hat{a}_{m,n} + \text{h.c.} \right), \quad (\text{S1})$$

where the operators $\hat{a}_{m,n}$ ($\hat{a}_{m,n}^\dagger$) annihilate (create) a particle on the lattice site $\ell = (m, n)$, where m and n denote the site indices along the x and y directions, respectively. The uniform flux per plaquette $\phi = 2\pi\alpha$ is defined modulo 2π . For a rational flux $\alpha = p/q$, with (p, q) prime numbers, the single-particle spectrum splits into q subbands. When represented as a function of the flux α , these energy bands form a fractal structure known as the Hofstadter butterfly.

The finite (uniform) flux per plaquette ϕ breaks time-reversal symmetry, hence leading to non-trivial topological properties: the Hofstadter bands are associated with a non-zero (first) Chern number. Considering the flux $\alpha = 1/4$ as an example, the HH model exhibits 4 subbands, with the middle two bands touching at singular (Dirac) points [Fig. S1(a)]. The lowest and the highest bands share the same Chern number $C = 1$; while the middle degenerate band is associated with the Chern number $C = -2$.

Under open boundary conditions, the model hosts chiral edge modes whose energies are located within the bulk energy gaps; these edge states can be identified in the red spectrum displayed in Fig. S1(b), where a steeper slope reflects the low density of (edge) states within the bulk gaps. Considering the flux $\alpha = 1/4$ (main text), the two bulk gaps each hosts a single edge mode. The chirality of these two edge modes are opposite: the edge mode located in the lowest (resp. highest) bulk gap propagates in a clockwise (resp. anti-clockwise) manner; see also Fig. 2(d) and (f) in the main text, where these two opposite chiral motions are revealed using the elevator scheme.

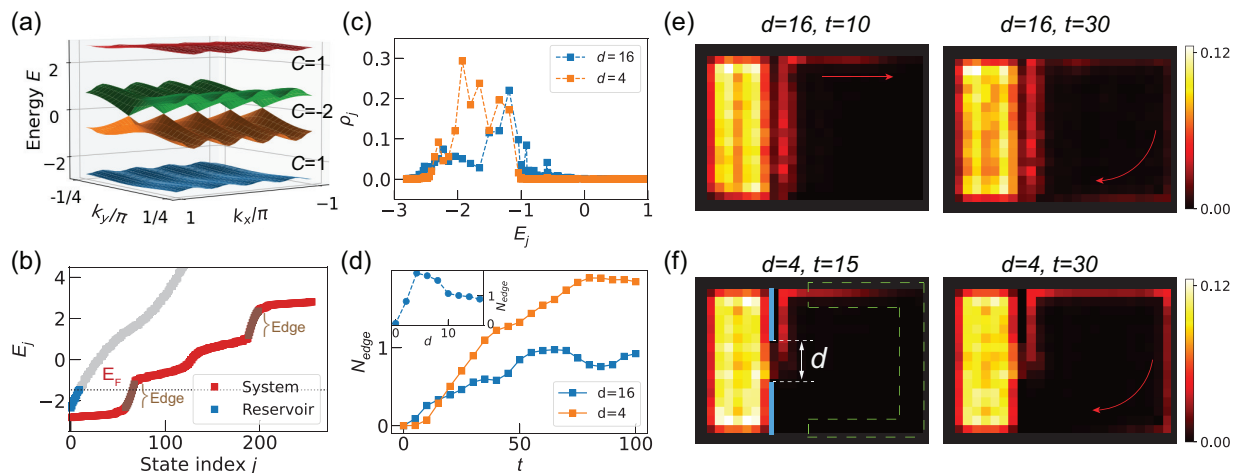


FIG. S1. **Edge state injection with a trivial reservoir.** (a) Energy spectrum as a function of quasimomenta k_x and k_y . We set the lattice constant $a = 1$. The Chern numbers of the separated bands are $C = 1, -2, 1$, respectively. (b) Energy spectrum as a function of the state indices. The blue and red dots correspond to the Hamiltonian describing the trivial reservoir (with chemical potential $\epsilon_R = 1.5$) and the Hofstadter system, respectively. We consider a trivial reservoir of size 7×16 which is coupled to a system of size 16×16 with flux $\phi = \pi/2$ per plaquette. A high wall (one site wide) is placed between the reservoir and the system [blue lines in (f)], which leaves a door of width d open in the middle. (c) Population of HH eigenstates ρ_j as a function of their energy E_j for different door width d , at time $t = 40$. (d) Number of the injected particles in the edge as a function of the time for different door width d . Inset: The number of particles in the edge as a function of d at $t = 100$. Snapshots of spatial density distribution for (e) $d = 16$, (f) $d = 4$. The green dashed line indicates the region used to count the number of particles at the edge, and the blue bonds represent the high wall. Initially there are $N = 10$ particles in the reservoir, and the on-site potential in the reservoir is suddenly lifted to the value $\epsilon_R = 1.5$. Energy and time are in units of J and \hbar/J , respectively. The arrows in (e) and (f) are a guide to the eye for the chiral motion.

II. EDGE-STATE INJECTION USING A TRIVIAL RESERVOIR

In the main text, we have shown that chiral edge states can be populated in an energy-selective manner, using a system-reservoir setting immersed in a uniform magnetic flux. In this Appendix, we show that a trivial reservoir (i.e. a reservoir without flux) can also be used to inject particles into the edge states of a quantum Hall system.

Similarly to the sketch in Fig. 1(a) in the main text, we couple a system described by the HH model to a reservoir without magnetic flux. Initially, the reservoir is filled with free fermions, and the system is empty. Suddenly lifting the reservoir on-site potential ϵ_R , such that the energy of the particles in the reservoir becomes resonant with an edge mode of the system [Fig. S1(b)], is found to generate chiral edge currents in the system [Fig. S1(e)]. Even though only a small fraction of particles are injected into the edge states in this case, we find that applying a high wall between the reservoir and the system, but leaving a small door open in the middle of the wall, can improve the efficiency. In Fig. S1(f), we plot the snapshots of density distributions of the time-evolved state using a small door opening of width $d=4$, from which we observe stronger chiral edge currents appearing in the system. We attribute the better efficiency of the door-opening configuration to the fact that a wider range of quasi-momenta is offered by a smaller door width, thus allowing for the population of more edge states in the system; see Fig. S1(c) where we plot the population of HH eigenstates for different d .

By monitoring the number of particles N_{edge} injected in a specific region of the edge [depicted by the dashed lines in Fig. S1(f)], we find that tuning the door width d manifests as a way of controlling the number of particles injected into the edge states, as shown in Fig. S1(d). In the inset of (d), we plot N_{edge} as a function of the door width d at time $t = 100$, and the optimal fraction of injected particles is found at a door width of intermediate size.

III. CHERN INSULATOR PREPARATION USING THE INJECTION SCHEME

Here, we investigate the possibility of preparing a CI based on injecting particles from a reservoir into an empty system. As an example, we partition a large box of size 12×12 into a sub-box of size 8×8 at the center (the “system”) and we define the rest as a trivial reservoir (without magnetic flux). The middle sub-box is our target system, described by the HH model with flux $\phi = \pi/2$ per plaquette. We first analyze the ground-state properties of such a system-reservoir setup. Figure S2(c) shows the bulk density n_B as a function of the reservoir potential ϵ_R . The incompressible nature of the CI ground state manifests as a plateau in the bulk density. Its topological nature can be confirmed from the local Středa’s marker shown by the red dots in Fig. S2(c), which forms a plateau around 1 in the region with bulk density saturation, which is in agreement with the Chern number $C = 1$ of the occupied lowest band.

Based on this ground-state property, one can envisage to adiabatically prepare a CI by slowly ramping up the reservoir potential ϵ_R . In our setup, such an adiabatic limit will be determined by the energy gap δE just above the Fermi level. A typical avoided-crossing is shown in the inset of Fig. S2(a), and the energy gap δE as a function of ϵ_R is plotted in Fig. S2(b). We find that, in order to build up a CI by ramping up ϵ_R , one has to pass through an energy gap as small as $\delta E = 0.0013$, which complicates the preparation in practice. The bulk density is plotted in Fig. S2(d) for different ramping times τ , upon using a linear ramping up of ϵ_R . It shows that thousands of tunneling times ($\sim 1/\delta E$) would be required to approach the adiabatic limit for this system size; see also the scaling shown in the inset of Fig. S2(b).

As regards the preparation of a large CI through particle injection, another difficulty concerns the presence of isolated eigenstates deep in the bulk of the system. Taking a box of size 20×20 as an example, we partition it into a target HH system of size 12×12 and define the rest as the reservoir. Considering an improved ramp (based on a saturation function), we obtain the eigenstate populations ρ_j displayed in Fig. S2(e). From the zoom-in plot in the inset, we identify several dips in the eigenstate populations: those dips correspond to eigenstates that are located deep in the bulk, and which are essentially isolated from the reservoir. The spatial density distribution of such a typical isolated eigenstate is shown in Fig. S2(e), with the red box indicating the boundary between the target system and the reservoir.

The existence of eigenstates located deep in the bulk, which are essentially decoupled from the reservoir, complicate the perfect filling of the target topological band. This issue can be solved by improving the system-reservoir coupling (e.g. by increasing the system-reservoir interface or considering a double-layer configuration), or by considering systems with (strong) interactions; see main text and Section IV below.

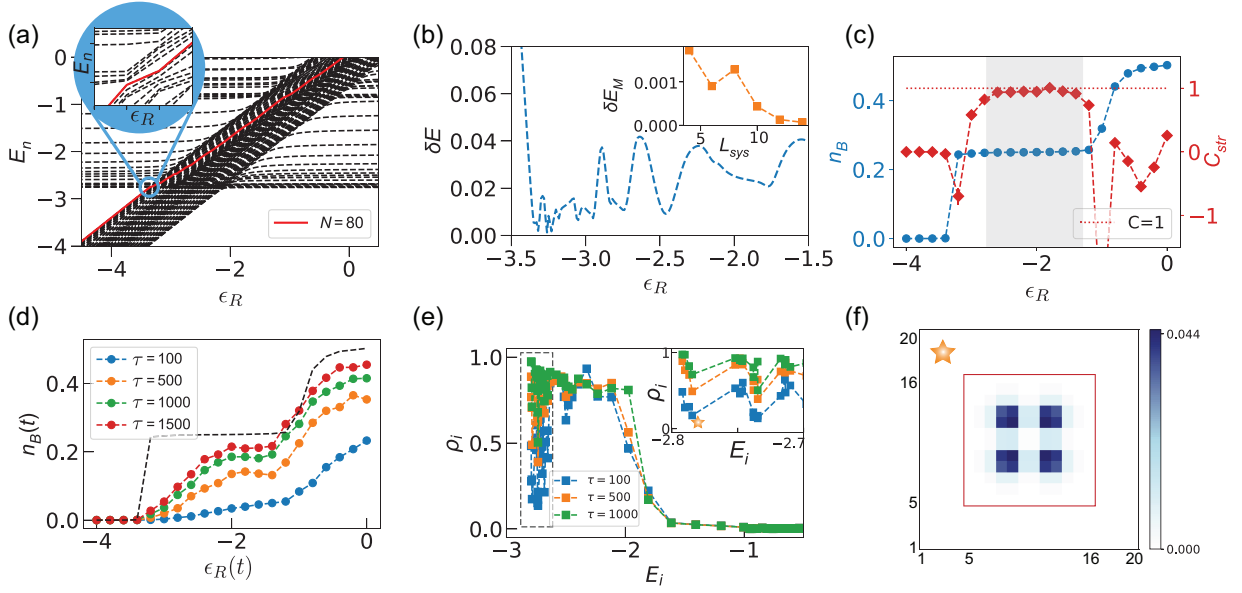


FIG. S2. **Preparing a Chern insulator based on injection.** (a) Energy spectra of the entire setup as a function of ϵ_R . The red line indicates the Fermi level. Considering a box of size 12×12 with a target system being a 8×8 sub-box at the center, the Fermi level corresponds to the 80th eigenvalue. (b) Energy gap (difference between the 80th and 81st eigenvalues) for $J_R=0.2$. The minimal energy splitting is found to be $\delta E_M=0.0013$. Inset: the minimal energy splitting δE_M as a function of the system length L_{sys} ; here, we consider square boxes of increasing size $L \times L$, and keep the ratio $L/L_{\text{sys}} \simeq 1.6$ constant. (c) The bulk density and the local Středa marker as a function of ϵ_R . The bulk density is evaluated within the central 2×2 sites. The shadow indicates the regime of Chern insulator ground states in the system. (d) The bulk density as a function of ϵ_R for different τ . The black dashed line is the ground state density shown in (c), which represents the adiabatic limit. Here we linearly ramp up ϵ_R from -4 until 0 within time τ , with the initial state being a fully filled trivial reservoir. (e) The population of the eigenstates of the Hofstadter model. Here we consider a bigger box of size 20×20 partitioned into the target system of size 12×12 and a reservoir. We ramp up ϵ_R from -4 until -2.5 by using a saturation function with time τ . Inset: zoom-in of heavy depletion region indicated by the dashed box. (f) The spatial density distribution of a typical isolated bulk state with index $j = 3$. Here, the tunneling strength is $J_R = 0.2$.

IV. FRACTIONAL CHERN INSULATOR PREPARATION USING THE INJECTION SCHEME

A. Using a linear ramp

Despite the difficulties mentioned above, injecting particles into an empty system can still be used to prepare a strongly-correlated FCI state, as demonstrated in Fig. 3 in the main text. The reasons are twofold. First, considering a small FCI droplet, the many-body gap across the injection process can potentially remain (reasonably) large due to finite size effects. Second, the strong interactions potentially prevent the isolation of bulk states, as previously illustrated in Figs. S2(e)-(f). As a further demonstration, here we show that a linear ramp of ϵ_R can also be used to prepare a small FCI droplet.

We start from a trivial state with 6 hard-core bosons in each reservoir, as shown in Fig. S3(a), leaving the system empty. After linearly ramping up the reservoir potential $\epsilon_R(t)$ from -3 until -2 within a duration τ , we track the bulk density, as evaluated within the central 2×2 sites, as a function of $\epsilon_R(t)$; see Fig. S3(d). One observes that the bulk density approaches the adiabatic-limit prediction for a sufficiently long ramping time. The sudden increase of the bulk density indicates a transition. As further confirmed by the local Středa marker in Fig. S3(e), the obvious dip (breakdown) of C_{str} indicates a change in the topological properties. By using sufficiently long ramping times, C_{str} gets close to the expected value $1/2$. The final Středa marker as function of total ramping time is plotted in Fig. S3(f), with the inset showing that a ramping time $\tau = 180$ leads to the marker's value $C_{\text{str}} \approx 0.59$.

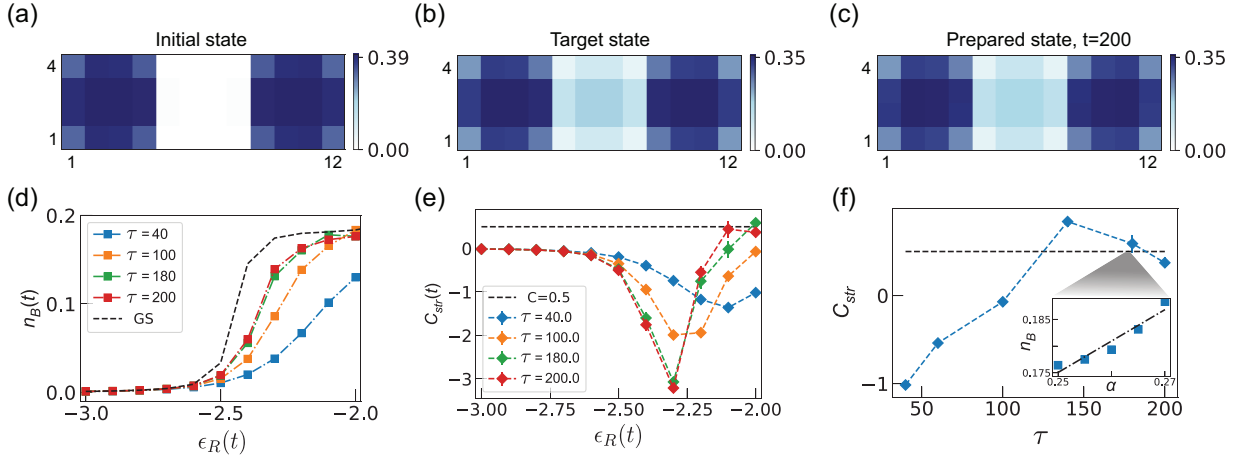


FIG. S3. **Preparing a fractional Chern insulator by using a linear ramp.** The spatial density distribution of (a) the initial state with $\epsilon_R = -3$, (b) the target state with $\epsilon_R = -2$ and (c) the prepared state at time $t = \tau = 200$. (d) The bulk density as a function of ϵ_R for different τ . The black dashed line corresponds to the adiabatic limit. (e) The local Středa marker $C_{\text{str}}(t)$ as a function of $\epsilon_R(t)$ for different τ . (f) The final Středa marker as a function of τ . Inset: linear fit of the density versus flux at $\tau = 180$, which gives $C_{\text{str}} \approx 0.59$. Here, we consider $N = 12$ hard-core bosons, and the system of size 4×4 is coupled with two reservoirs with $J_R = 0.15$, each of which has size 4×4 . The error bars denote the standard error of a regression slope.

B. Finite size effects

After demonstrating the validity of our injection scheme for the preparation of a small FCI, we now analyze how the efficiency of this scheme scales with the size of the reservoir, as well as with the size of the target system. Focusing on the sub-box configuration introduced in Fig.3(a) of the main text, we consider a target system of size $L_S \times L_S$ coupled with two identical reservoirs of size $L_R \times L_S$, where L_S and L_R denote the lengths of the system and reservoir, respectively.

We first investigate the effects of the reservoir length L_R by fixing $L_S = 4$ and the total particle number $N = 12$. We calculate the many-body gap ΔE as a function of the reservoir energy ϵ_R , within the range $-3 \leq \epsilon_R \leq -2$, where a transition is known to occur (see Fig. 3 in the main text). From this, we extract the minimal many-body gap ΔE_M , which sets the time-scale for adiabatic state preparation. The resulting quantity ΔE_M is plotted as a function of L_R in Fig. S4(a). We find that for $L_R \geq 3$, the minimal gap ΔE_M linearly decreases with L_R . Besides, by fixing $L_S = L_R = 4$, we find a non-linear increase of ΔE_M as a function of the total particle number N ; see Fig. S4(b). Since the value of the minimal gap ΔE_M determines the time scale for a possible adiabatic state preparation, the results presented here indicate that it is favorable to consider a reservoir of small size with many particles.

We now analyze how the size of the system L_S influences the efficiency of the scheme, by fixing the reservoir length $L_R = 4$ and the particle number $N = 12$. As shown in Fig. S4(c), the minimal gap decreases with L_S , which signals the potential difficulty of preparing an FCI in a substantially larger lattice system. This limitation could be circumvented by optimizing the reservoirs (see above), or possibly, by combining the injection scheme with the cleaning method described in the main text. Another route for improvement could be offered by a double layered system-reservoir configuration; in practice, this could also be realized using two different internal states of an atom for the system and reservoir, respectively.

Last but not least, we analyze the (ideal) particle density expected within the bulk of the system n_B as a function of the system size L_S , for a fixed reservoir energy $\epsilon_R = -2$; see Fig. S4(d). It is interesting to note that the particle density n_B already approaches its thermodynamic-limit value $n_B = \nu\alpha = 1/8$ (expected for a $\nu = 1/2$ Laughlin state) for a system size $L_S \gtrsim 8$. Specifically, we find $n_B \simeq 0.127$ and $n_B \simeq 0.124$ for $L_S = 8$ and $L_S = 10$, respectively.

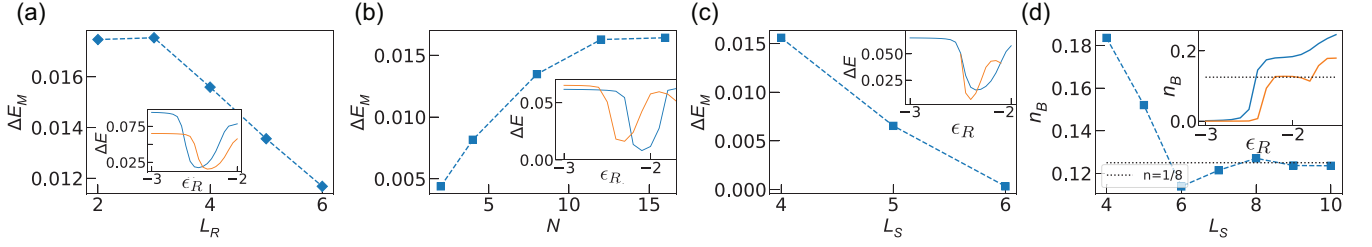


FIG. S4. **Finite size effects in the FCI-reservoir setup.** (a) The minimum gap ΔE_M as a function of the length of each reservoir L_R for a fixed total number of particles $N = 12$. Inset: The many body gap ΔE as a function of ϵ_R for $L_R=3$ (blue) and 4 (orange). (b) The minimum gap ΔE_M as a function of particle number N for a fixed $L_R = 4$. Inset: ΔE as a function of ϵ_R for $N=4$ (blue) and 12 (orange). In (a,b) we fix the system length $L_S = 4$. (c) The minimum gap ΔE_M as a function of the system length L_S for fixed $L_R = 4, N = 12$. Inset: ΔE as a function of ϵ_R for $L_S=4$ (blue) and 5 (orange). (d) The bulk density n_B as a function of L_S at $\epsilon_R = -2$ for $L_R = 4, N = 12$. Inset: n_B as a function of ϵ_R for $L_S = 4$ (blue) and $L_S = 8$ (orange). The dotted line indicates the expected $n = 1/8$ in the thermodynamic limit. The bulk density is averaged over a disk of radius $r = 1$ at the center of the system. In (a-d), we choose the width of the whole setup to be $W = L_S$ and use $J_R = 0.15, \alpha = 1/4$. The dashed lines are the guide to the eye.

V. STATE PREPARATION VIA REPEATED CLEANING

A. Rabi cycles

The aim of this Appendix is to estimate optimal parameters for the vacuum-cleaning scheme, by analyzing a simplified few-level model.

In Fig. 4(a) of the main text, we presented a sketch of a simplified 3-level toy model for our system-reservoir setup. Our aim is to gain more intuition on our repeated cleaning protocol by analyzing the Rabi oscillations that occur between these levels upon coupling them. To be specific, we introduce the Level-0, Level-1, and Level- R to denote our (target) lowest Chern band, the first excited band and the reservoir band, respectively. The corresponding characteristic energies are represented by E_0 , E_1 and ϵ_R in Fig. 4(a). Level-0 and Level-1 have the same coupling strength J_R with Level- R .

Starting from the situation where both the lowest and the excited bands are fully occupied, we aim to activate a coupling that keeps the lowest band occupation essentially unaffected, while cleaning off the population in the excited bands as much as possible. Specifically, in terms of the 3-level toy model, we analyze the occupation in Level-0 when the transition from Level-1 to Level- R is maximal. Here, we treat the 3-level toy model as two independent two-level systems: one describing the coupling of the reservoir to Level-0 and the other describing the coupling of the reservoir to Level-1.

In a two-level quantum system, it is well-known that the Rabi formula describes the transition from one level to the other. Starting from a state initially occupying the first level (denoted by a), the transition probability to the second level (denoted by b) reads

$$P_{ab}(t) = \frac{\gamma^2}{\gamma^2 + (E_a - E_b)^2/4} \sin^2 \left(\sqrt{\frac{(E_a - E_b)^2}{4} + \gamma^2 t} \right), \quad (\text{S2})$$

where E_a, E_b represent the level energies and γ is the strength of coupling between these two levels.

We first analyze the transition from Level-1 to Level- R , and we establish its optimal regime by finding the maximal value $P_{1R}^{\text{Max}} = P_{1R}(t^*)$ using Eq. S2; the time t^* will denote the optimal duration of the coupling. We plot P_{1R}^{Max} for different values of ϵ_R, J_R in Fig S5(a). When ϵ_R becomes resonant with $E_1 \simeq -0.6$, which is taken as the mean value of the excited Hofstadter band, the transition probability P_{1R} can take a value as large as 1. In order to study the remaining population in the Level-0 when P_{1R} is maximal, we plot $1 - P_{0R}$ at time $t = t^*$ in Fig S5(b).

Now, to identify an optimal regime for our control parameters, we define a figure of merit \mathcal{P} as

$$\mathcal{P} = 1 - P_{0R} + P_{1R}. \quad (\text{S3})$$

In the ideal case where the population in Level-1 is completely removed ($P_{1R} = 1$) while Level-0 remains perfectly unaffected ($P_{0R} = 0$), one has the maximal value $\mathcal{P} = 2$; vice versa one has the minimal value $\mathcal{P} = 0$. As shown in Fig. S5(c), it is preferable to set ϵ_R close to resonance with the excited band E_1 and to use a small coupling strength J_R , in order to empty the Level-1 while protecting the Level-0.

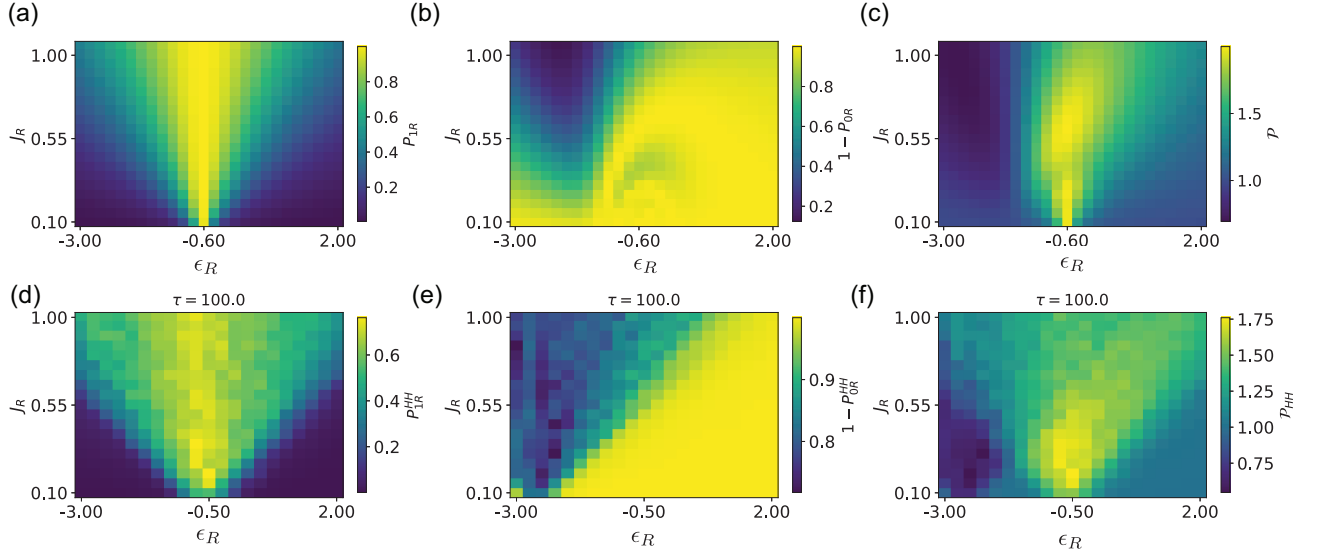


FIG. S5. **Rabi oscillations and quench dynamics.** (a) The maximal transition P_{1R}^{Max} , (b) the transition left in Level-0 $1 - P_{0R}$ at $t = t^*$, and the characteristic population \mathcal{P} of the simplified 3-level toy model. (d) The excited band transition P_{1R}^{HH} , (e) the remaining lowest band population $1 - P_{0R}^{\text{HH}}$, and the characteristic population \mathcal{P}_{HH} of the quench dynamics of our system-reservoir configuration at $t = 100$.

To make a further step towards our cleaning protocol, we now check the above-mentioned optimal parameter regime for a quench dynamics of our system-reservoir setup. Considering an initial state with 1/2-filling per site within the HH system (the central sub-box), we investigate the quench dynamics by suddenly setting ϵ_R to a given value. Similarly, we now define the figure of merit \mathcal{P}_{HH} for our HH system as,

$$\mathcal{P}_{\text{HH}} = 1 - P_{0R}^{\text{HH}} + P_{1R}^{\text{HH}}, \quad (\text{S4})$$

where we can express the possibility of transition from band i to the reservoir in terms of the eigenstate populations ρ_j as

$$P_{iR}^{\text{HH}} = \sum_{j=1}^{N_i} (1 - \rho_j) / N_i, \quad (\text{S5})$$

with $i = 0, 1$ and N_i being the number of bulk states belonging to band i . By plotting the figure of merit \mathcal{P}_{HH} for different values of J_R, ϵ_R in Fig. S5(f), one identifies an optimal parameter regime, where ϵ_R is close to the mean energy value E_1 of the excited band and where the coupling J_R is relatively weak. In contrast, when ϵ_R is set close to the mean energy of the lowest band $E_0 \simeq -2.7$, a small \mathcal{P}_{HH} is found due to a heavy depletion of the lowest band. When ϵ_R is set to a very large value (off resonance), no transition takes place between the system and the reservoir, and thus \mathcal{P}_{HH} saturates to 1. This analysis shows a qualitative agreement with the simplified Rabi model [Fig. S5(c)].

B. Dynamical cleaning scheme and scaling

Despite the identification of an optimal parameter regime (see above), a simple quench dynamics does not lead to a satisfactory preparation of the CI, i.e. a complete depletion of the excited bands while leaving the lowest band perfectly filled. This is essentially due to the finite dispersion of the HH bands. To solve this issue, we consider tuning ϵ_R in a time-dependent fashion, as we now explain.

We choose to dynamically tune the reservoir potential according to a saturation function,

$$\epsilon_R(t) = \epsilon_R^i - (\epsilon_R^i - \epsilon_R^f) t / (\sqrt{c\tau^2 + t^2}), \quad (\text{S6})$$

with the initial value $\epsilon_R^i = 4$, a constant parameter $c = 0.02$ and the total ramping time τ . As shown in Fig. S6(a), after reaching the final value ϵ_R^f , we quickly lift ϵ_R to a high value. Since the system is now almost completely

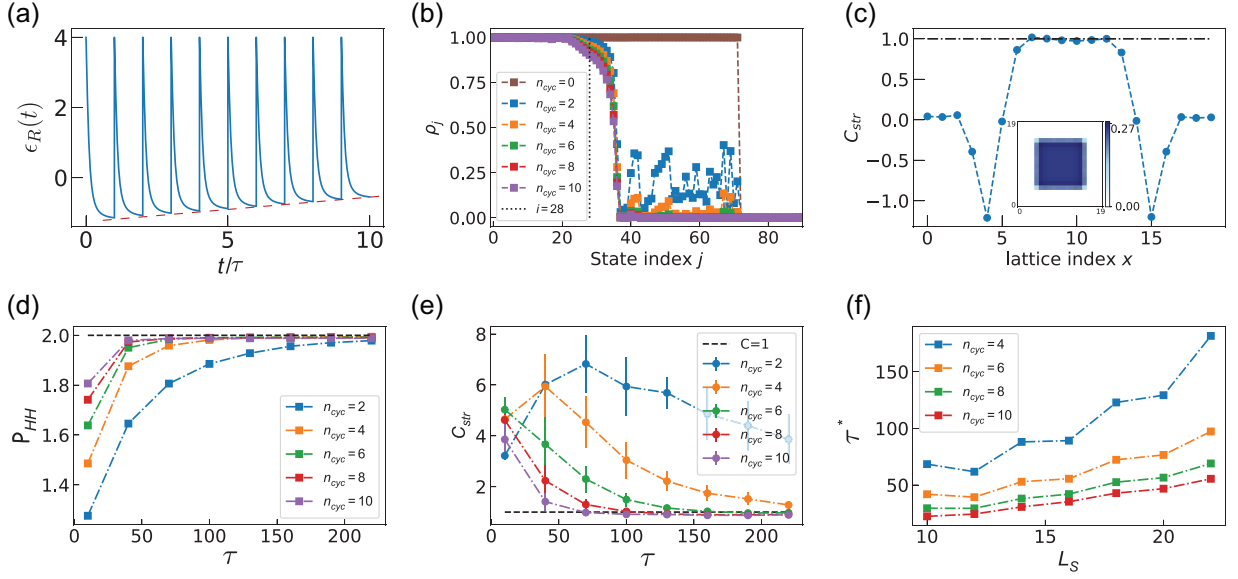


FIG. S6. **Preparing a Chern insulator based on cleaning.** (a) The repeated ramping protocol for ϵ_R according to a saturation function. The red dashed line is the guide to the eye. (b) Population in HH eigenstates for different n_{cyc} with $\tau = 70$ per cycle. (c) The local Středa marker of the evolved state with $n_{\text{cyc}} = 10, \tau = 70$ as a function of lattice indices along the middle row. Inset: the corresponding spatial density distribution of the evolved state. (d) The characteristic population \mathcal{P}_{HH} as a function of τ for different cycles n_{cyc} . (e) The local marker as a function of τ for different cycles n_{cyc} and L_S . The local marker is averaged over a disk at the center with a radius of $r = 2$. The error bars denote the standard error of a regression slope. (f) The typical time τ^* as a function of the system length L_S . During the scaling, we consider square boxes and keep the length ratio between the whole set up and the system as $L/L_S \simeq 1.6$. For (b-e), we partition a lattice of size 20×20 into a target 12×12 system (central box) and a surrounding reservoir with particle number $N = 72$. We set a flux $\phi = \pi/2$ in the system and $\phi = 0$ in the reservoir, and use $J_R = 0.15, \xi = 3$.

decoupled from the reservoir, one can easily remove the particles from the reservoir. The ability of preparing such an empty reservoir makes it possible to have several cycles. To increase the efficiency, one can design the final value of ϵ_R^f for each cycle n_{cyc} as

$$\epsilon_R^f(n_{\text{cyc}}) = \epsilon_R^f(1) + J_R \xi \frac{n_{\text{cyc}} - 1}{N_{\text{cyc}} - 1}, \quad (\text{S7})$$

with $n_{\text{cyc}} = 1, \dots, N_{\text{cyc}}$ and N_{cyc} is the total cycle number. The coefficient ξ controls the final value of ϵ_R . For the very first cycle, we take $\epsilon_R^f(1) = -1.14$ which is located right below the excited band.

Considering a many-body state at $1/2$ -filling as our initial state, we now apply our repeated cleaning protocol to prepare a CI in the system: we aim at removing the higher band populations but leaving the lowest Chern band almost perfectly filled. As shown in Fig. S6(b), we find an efficient depletion of the excited bands with the increase of the cycle number. During the ramp, the bulk states of the lowest band remain almost perfectly filled. This already points towards the realization of a CI state in the system. To further confirm its topological nature, we plot the local Středa marker (averaged over the surrounding 4 sites) for $n_{\text{cyc}} = 10$ with $\tau = 70$ per cycle in Fig. S6(c), which shows a uniform bulk with $C_{\text{str}} \approx 1$. By plotting the figure of merit \mathcal{P}_{HH} , and the Středa marker in Fig. S6(d) and (e), respectively, we find an efficient cleaning for $\tau \gtrsim 70$ and $n_{\text{cyc}} \approx 10$ cycles, or $\tau \gtrsim 100$ and $n_{\text{cyc}} \approx 8$ cycles. This illustrates how using more cycles would help reducing the total preparation time. Besides, in order to appreciate the scaling behavior, we plot a typical time τ^* corresponding to a figure of merit \mathcal{P}_{HH} above 1.95 in Fig. S6(f). We find that the typical time per cycle increases more slowly with the system size as one increases the number of cycles.

C. Full preparation protocol using the cleaning scheme

In the main text, we apply our repeated cleaning protocol to a realistic state, which has been prepared starting from a trivial metal (i.e. starting from a band structure with zero Chern numbers). Here we give more details about the full ramping protocol.

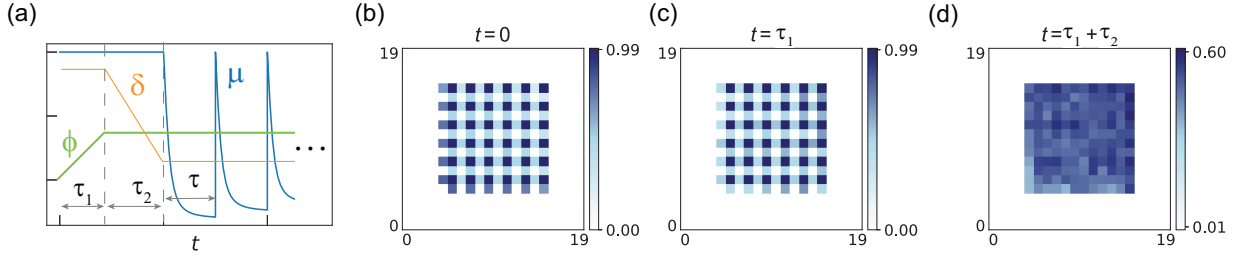


FIG. S7. **Full protocol for preparing CI based on cleaning** (a) The full protocol for ramping system parameters. The flux is linearly increased from 0 to $\pi/2$ within τ_1 , and then we decrease the staggered potentials δ from 20 to 0 within τ_2 . After that, we apply our cleaning protocol cycle by cycle with τ being the ramping time per cycle. (b-d) The spatial density distributions at $t = 0, \tau_1$ and $\tau_1 + \tau_2$, respectively. Here, we use time $\tau_1 = \tau_2 = 100$ for tuning ϕ and δ .

We start from a trivial metal in the presence of a large staggered potential, $\delta_\ell = [(-1)^m + (-1)^n]\delta/2$, with (m, n) being the lattice indices along x and y direction, respectively. We then linearly ramp up the flux in the lattice from 0 to the value of $\pi/2$. Since the system is still within a trivial regime (guaranteed by the large staggered potentials $\delta = 20$), one can ramp up the flux rather quickly. After that, we slowly reduce the staggered potential in order to change the topological nature of the bands; this transition generates excitations in the higher bands for a realistic quasi-adiabatic ramp; see the sequence in Fig. S7(a). The density distribution of the evolved state, across the topological phase transition, is shown in Fig. S7(b)-(d); this latter situation corresponds to the blue dots in the band populations shown in Fig. 4(b) in the main text.

With this realistic (but highly excited) state in hand, we now apply our repeated cleaning protocol. In order to progressively address the higher bands at each cycle, we set $\epsilon_R^f(1) = -1.14$ and $\xi = 14$ for the final value of ϵ_R^f defined in Eq. (S7); see also Fig. S7(a). In this case, the final value of ϵ_R^f in the last cycle reads 0.94, which is located near the top of the excited band. Note that even though we only consider a linear increase of ϵ_R^f at each cycle (for simplicity), a more efficient protocol could be designed by fine tuning ϵ_R^f within each cycle, e.g. by means of optimal control or even machine learning.